ADVANCED FUNCTIONAL MATERIALS
www.afm-journal.de

# Sensing Mucus Physiological Property In Situ by Wireless Millimeter-Scale Soft Robots

*Boyang Xiao, Yilan Xu, Steven Edwards, Lohit Balakumar, and Xiaoguang Dong**

**The physiological property of mucus is an important biomarker for monitoring the human health conditions and helping understand disease development, as mucus property such as viscosity is highly correlated with inflammation and other diseases. However, it remains challenging to sense mucus viscosity using pure medical imaging. Collecting and analyzing mucus sample in vitro using flexible endoscopes and capsule endoscope robots is also challenging due to their difficulty of accessing very confined, tortuous, and small spaces, and the sample may not reflect the real mucus property. Here a novel method is proposed to enable sensing mucus viscosity in situ by wireless miniature sensors actuated by magnetic fields and tracked by medical imaging. These miniature viscosity sensors can be delivered with minimal invasion using a novel sensor delivery mechanism by controlling a magnetically actuated millimeter-scale soft climbing robot. As the soft robot can access confined and narrow spaces, and reliably deploy the sensor on soft tissue surfaces, multiple sensors can be delivered on soft biological tissues to sense biofluid viscosity spatiotemporally. The proposed minimally invasive robotic delivery and viscosity sensing method thus paves the way toward sensing biofluid properties deep inside the body for future disease monitoring and early diagnosis functions.**

## 1. Introduction

Constructing a sensor network on soft biological tissues could help continuously monitor physiological properties of soft tissues in situ, facilitate the understanding of disease development, and provide a long-term diagnosis function.[1,2] The human gastrointestinal (GI) and respiratory tracts are covered with mucus which is a complex biological fluid that lubricates and protects the mucosa layer.[3,4] Mucus has a viscosity ranging from 100 to 10 000 times the viscosity of water, which is an important biomarker for monitoring human physiological properties and enabling early disease diagnosis.[4–6] Particularly in the GI tract, compared with that in healthy people, mucus viscosity is evidently different for patients with peptic ulcer,[7,8] inflammatory bowel disease (IBD)[9,10] and unbalanced gut microbes.[11] Mucus viscosity will also increase when viscous and thick mucus is built up for patients with cystic fibrosis (CF)[12–15] due to genetic problems. Monitoring mucus viscosity continuously could help understand the development of disease and help identify efficient point-of-care treatment methods by providing continuous feedback information.

However, it is challenging to measure mucus viscosity using existing medical imaging modality and medical tools. GI tract endoscope-based procedures such as endoscopic retrograde cholangiopancreatography (ERCP)[16] or colonoscopy[17] cannot access the small intestine and upper colon easily and can potentially cause trauma and other complications for patients under anesthesia.[18,19] In addition, passive capsule devices[20–23] and mobile capsule endoscope robots[24–29] have been developed to collect and sense biofluids in the GI tract,[30,31] which are typically at the centimeter scale and can only access the space with comparable size of the capsule in the GI tract.[32] Moreover, further in vitro testing of the properties of the collected mucus sample using fluorescence microscopes and other tools[33] may not accurately reflect the mucus properties as they depend on the environment humidity and temperature.[3] Therefore, wireless sensors delivered with minimal invasion that can sense mucus properties in situ are demanded[2,31,34,35] for continuously sensing mucus viscosity for disease monitoring and diagnosis. However, such miniature wireless sensors are currently missing, and the method to deliver these sensors onto mucus-covered soft tissues deep inside the body is also limited.

To tackle this challenge, we propose a method to sense mucus viscosity in situ enabled by wireless miniature viscosity sensors actuated by magnetic fields and tracked by medical imaging. We also propose a novel delivery mechanism for the miniature sensors by controlling millimeter-scale soft climbing robots. First, we present the delivery mechanism by introducing the design,

B. Xiao, Y. Xu, L. Balakumar, X. Dong
Department of Mechanical Engineering
Vanderbilt University
Nashville, TN 37240, USA
E-mail: xiaoguang.dong@vanderbilt.edu
B. Xiao, Y. Xu, X. Dong
Vanderbilt Institute for Surgery and Engineering
Vanderbilt University
Nashville, TN 37240, USA
S. Edwards, X. Dong
Department of Biomedical Engineering
Vanderbilt University
Nashville, TN 37240, USA

The ORCID identification number(s) for the author(s) of this article can be found under https://doi.org/10.1002/adfm.202307751

**DOI: 10.1002/adfm.202307751**

 

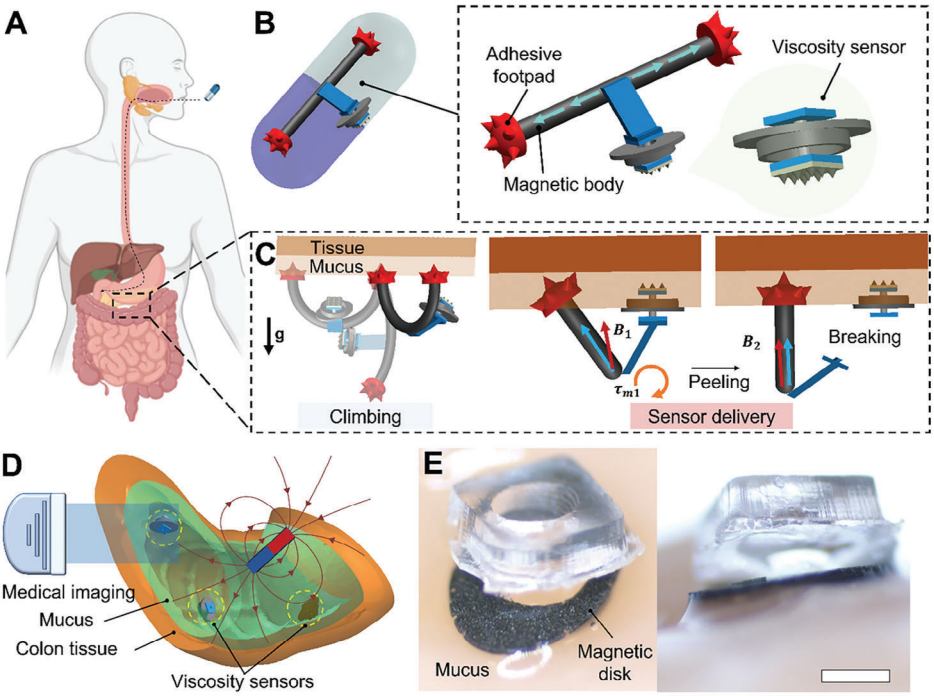


**Figure 1.** Soft climbing robot enabled delivery of wireless miniature sensors for in situ sensing of mucus viscosity. A) Concept of a millimeter-scale soft robot for sensor delivery encapsulated by a swallowable capsule. B) Illustration of the soft climbing robot and viscosity sensor to be encapsulated in a capsule. The blue arrows on the magnetic robot body indicate its magnetization profile. The components of the viscosity sensor include a magnetic spinner, an adhesive patch for anchoring, and a shaft for rotational motion. C) Illustration of the climbing motion and deployment of the magnetic viscosity sensor on a mucus-covered soft tissue surface by controlling a soft climbing robot. D) Illustration of the deployment and tracking of multiple viscosity sensors for monitoring mucus viscosity spatiotemporally under medical imaging. E) Images of a viscosity sensor anchored on porcine colon tissue with direct contact to the mucus layer. Scale bar, 500 μm.

fabrication, and control of a miniature soft robot for climbing soft biological tissues with agile maneuverability. Second, we explain the delivery of sensors by the soft robot on soft biological tissues covered with mucus. Moreover, we further show the design and characterization of the magnetically actuated viscosity sensor for sensing liquid viscosity in synthetic fluids enabled by the fluid-structure interaction. Finally, we demonstrate controlling the soft robot to deliver multiple viscosity sensors on the porcine colon tissues ex vivo to sense mucus viscosities spatiotemporally. The major innovation in this work is that we propose a novel mechanism for delivering wireless miniature sensors by controlling millimeter-scale soft climbing robots in a minimally invasive manner. In addition, we report a novel wireless miniature sensor that can sense mucus properties on biological tissue surfaces deep inside the organs. The proposed minimally invasive robotic delivery mechanism and viscosity sensing devices could potentially allow sensing biofluid properties deep inside the body with minimal invasion for disease monitoring and diagnosis functions in the future.

## 2. Results

### 2.1. Concept of In Situ Viscosity Sensing Enabled by Soft Miniature Robots

**Figure 1** shows the concept of the wirelessly actuated viscosity sensor for sensing mucus viscosity in the GI tract and its delivery mechanism by a soft climbing robot capable of navigating on soft tissues. The soft climbing robot carrying a viscosity sensor can be encapsulated in an ingestible capsule to reach the deep area of the GI tract such as the large intestine as shown in Figure 1A. When the robot is released from the capsule after dissolving, it could be further controlled by external magnetic fields to navigate to a targeted position to deploy the viscosity sensor. Figure 1B illustrates the viscosity sensor and the soft climbing robot which has a rod-shaped magnetic body with a specific magnetization profile, two adhesive footpads, and a mechanical structure for delivering the viscosity sensor (see Figure S1 and Table S1 for the dimensions, Supporting Information). The robot and sensor are manufactured by combining laser machining and micro-molding (see Figure S2, Supporting Information, and the "Experimental Section" for more details). The viscosity sensor has a magnetic spinner that rotates about a shaft, and an adhesive patch with microspikes for anchoring on mucus-covered soft tissues which will be discussed in "Mechanism of Wirelessly Sensing Liquid Viscosity".

The soft climbing robot can climb a soft and wet tissue surface by a previously reported peeling-and-loading mechanism[36] and a chitosan-based bioadhesive[37] coated on the robot footpads for adhering to the mucus layer. The robot exhibits agile maneuverability by controlling the external magnetic fields (see "Robot Locomotion and Sensor Delivery on Mucus-Covered Biological Tissues"). Figure 1C shows that the soft robot can reach the targeted position through the climbing motion and the viscosity

 

sensor can be deployed and anchored onto mucus-covered biological tissue surfaces by controlling a delivery beam on the soft robot, which allows the sensor to be pushed onto soft tissues and detach from the delivery beam due to a breaking mechanism. Moreover, medical imaging modalities such as X-ray imaging can be used to guide the navigation of the soft climbing robot and track the magnetic spinner for sensing mucus viscosity as shown in Figure 1D. Multiple sensors can be deployed sequentially by the miniature soft climbing robots to build a sensor network on the soft tissues. Each sensor can work individually when actuated by a rotating magnetic field so that the sensor can be used for monitoring mucus viscosity spatiotemporally such as the viscosity sensor anchored on a porcine colon tissue shown in Figure 1E.

### 2.2. Robot Locomotion and Sensor Delivery on Mucus-Covered Biological Tissues

We present the robot locomotion mechanism on mucus-covered tissues for the rod-shaped soft robot when carrying a cantilever delivery beam in **Figure 2**. Figure 2A shows that the robot can bend in arbitrary directions when actuated by a 3D external magnetic field $\boldsymbol{B}$ after one robot footpad adheres to the tissue surface due to bioadhesion. The robot climbing locomotion is enabled by our previously reported peeling-and-loading mechanism.[36] As shown in Figure 2B, when peeling a footpad from the tissue, a magnetic torque in the plane of the robot body is generated on the robot body by rotating the external magnetic field. The magnetic torque further induces a force couple applied on the robot footpads. By increasing the magnetic torque, the peeling force of the detaching footpad will be greater than the anchoring force leading to the detachment. When loading a footpad, an opposing magnetic torque generated by rotating the magnetic field is applied to make the robot bend toward the tissue surface. The magnetic torque also produces the loading force required to adhere the footpad on the tissue surface. Figure 2C and Movie S1 (Supporting Information) show the control of the inverted climbing process of the soft robot on porcine colon tissues. When one robot footpad adheres to the soft tissue, the other robot footpad is free at the beginning ($t = 0$ s). The unanchored footpad is loaded on the tissue surface by rotating the external magnetic field ($t =$ 9 s). Then, the other footpad is peeled off from the tissue surface ($t = 48$ s). After the peeling process, the robot still has one footpad adhering to the tissue and can be again steered to the targeted directions by controlling the angle of the external magnetic field ($t$ = 51 s and $t = 75$ s). In addition, we also verify that the robot locomotion on the porcine colon tissue is minimally affected by pH after being tested in the simulated gastric fluid (SGF) (Figure S3, Supporting Information).

To illustrate the sensor delivery mechanism, in Figure 2D–H, we show the sensor delivery mechanism and estimation of the peeling and loading forces generated by the net magnetic torque. Before the sensor deployment, the robot first moves to the targeted position and loads its two footpads on the tissue surface. As shown in Figure 2D and Movie S2 (Supporting Information), we apply a magnetic torque to load the sensor on the mucus layer by rotating the magnetic field out of the robot plane at $t = 17$ s. After the sensor contacts the tissue surface, the magnetic torque induces a peeling force on the robot footpads and a loading force on the viscosity sensor. After applying the loading force for 60 s to ensure sufficient tissue adhesion, an opposing magnetic torque is exerted to induce a breaking force between the viscosity sensor and the delivery beam ($t = 160$ s). When further rotating the magnetic field, the pulling force applied to the delivery beam increases and becomes sufficient to overcome the friction between the rod on the delivery beam and the hole on the viscosity sensor. The viscosity sensor starts to slide and is detached from the delivery beam ($t = 215$ s). The viscosity sensor remains on the tissue surface due to the strong bioadhesion from the mucus layer ($t =$ 237 s). In Figure 2E,F, we present the magnetic field waveform including the magnitude $B$ and angle $\alpha_B$ in the delivery process, respectively. At the same time, the robot body angle $\alpha_r$ is extracted from the optical images to further analyze the applied magnetic torque, as well as the induced surface adhesion and supporting force on the robot footpads and sensor adhesive patch. Assuming only rigid-body rotation, based on the moment balancing condition of the robot and sensor, the adhesion and supporting force are given by,

$$F_a = F_n = \tau_m / d \tag{1}$$

where $d$ is the distance between the midpoint of the two robot footpads and the sensor adhesive patch, and $\tau_m$ is the magnetic torque given by $\tau_m = |\boldsymbol{m}_{net} \times \boldsymbol{B}| = m_{net} B \sin(\alpha_B - \alpha_r)$. Here $\alpha_r$ is the tracked robot body angle as shown in Figure 2G, and $\boldsymbol{m}_{net}$ is the net magnetic moment of the robot body which is obtained by tracking the robot deformed body shape and a known magnetization profile. Figure 2H shows the estimated time-varying adhesion where the negative peak value (−0.5 mN) indicates the breaking force required for sensor delivery. During this process, the adhesion on the sensor patch should be larger than this peak force to prevent the detachment of the sensor from the tissue surface.

To optimize the sensor anchoring force and robot maneuverability, we first investigate the design of the robot delivery beam for maximizing the sensor-tissue adhesion. We want to maximize the loading force $F_n$ as the adhesion between the viscosity sensor and the tissue is stronger with a larger loading force. Equation 1 indicates that the distance $d$ needs to be minimized for a maximum loading force as shown in **Figure 3**A. With a given $\theta_b$ and the robot height $h_r$ when deformed, the minimum $d$ is determined by $d_{min}^2 = (h_r \sin\theta_b)^2 - h_s^2$, where $h_s$ is the height of the sensor and $h_r$ is the assumed height of the deformed robot body when B = 20 mT. Meanwhile, we also want to minimize $L_b$ so that the delivery beam does not interfere with the robot climbing locomotion. To explore the feasible $\theta_b$ for the sensor delivery, we choose 30°, 45°, and 60° to quantify the maximum loading force and corresponding beam length for different $\theta_b$ in Figure 3B. If the delivery beam is too long as shown in Figure 3C ( $\theta_b = 30°$), the viscosity sensor may unintentionally touch the tissue when moving to a targeted location. Therefore, the maximum beam length is set to $0.75h_r$ to ensure the locomotion is not affected. When $\theta_b = 60°$, the loading force is not able to generate sufficient adhesion for the sensor deployment and the maximum adhesion is smaller than the breaking force so that the sensor will be detached from the tissue surface before breaking. When $\theta_b =$ 45°, the generated adhesion is sufficient for sensor deployment and the robot locomotion is not affected.

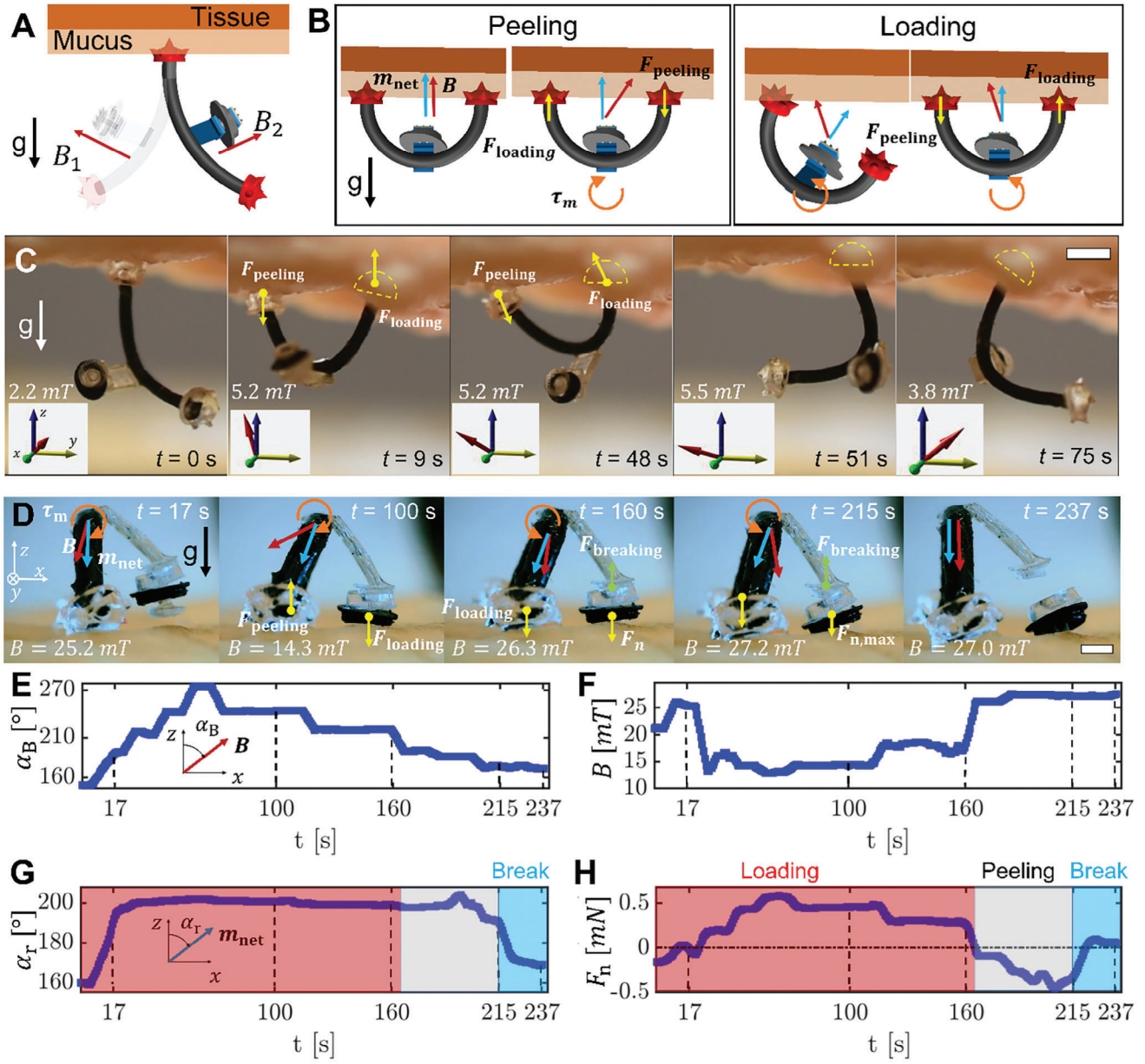


**Figure 2.** Controlling the robot climbing locomotion and the loading of viscosity sensors on soft tissues. A) Illustration of the omnidirectional steerability of the soft climbing robot on soft tissues by applying magnetic fields in different directions. B) Illustration of the peeling-and-loading mechanism to enable climbing on mucus-covered soft tissues. Yellow arrows: contact force. Blue arrows: net magnetic moment. Red arrows: external magnetic field. Orange arrows: magnetic torque. C) Video snapshots (Movie S1, Supporting Information) of the robot climbing locomotion on porcine colon tissues and the applied magnetic field in 3D. Scale bar, 2 mm. D) Video snapshots (Movie S2, Supporting Information) of the sensor-delivery process using the soft robot. Scale bar, 1 mm. E) The angle between the external magnetic field and *z*-axis as a function of time during the delivery process. F) The external magnetic field magnitude as a function of time during the delivery process. G) The angle between robot body plane and the *z*-axis as a function of time during the delivery process. H) The normal force applied on the sensor adhesive patch by the tissue surface as a function of time in the delivery process.

We then investigate the design of the rod-hole connection for controllable sensor loading and deployment. Figure 3D shows another design parameter – the ratio between the rod diameter $D_r$ and hole diameter $D_h$. The ratio $D_r/D_h$ determines the required breaking force for sensor deployment and should be within a range that allows controllable detachment without unintentional drop-off of the sensor during robot climbing. Figure 3E, F show the breaking force for different $D_r/D_h$ where $D_r$ is 0.59, 0.62, and 0.65 mm when $D_h$ is 0.6 mm. Figure 3E shows that when $D_r/D_h = 0.98$, the friction is insufficient so that the sensor may accidentally drop off before being loaded on the tissue. A minimum breaking force about0.4 mN is needed to avoid unplanned deployment. With $D_r/D_h = 1.08$, the friction is larger than the maximum breaking force or the maximum normal adhesion force between the sensor and mucus, making it unable to deploy the sensor. Thus, the maximum required breaking force is estimated to

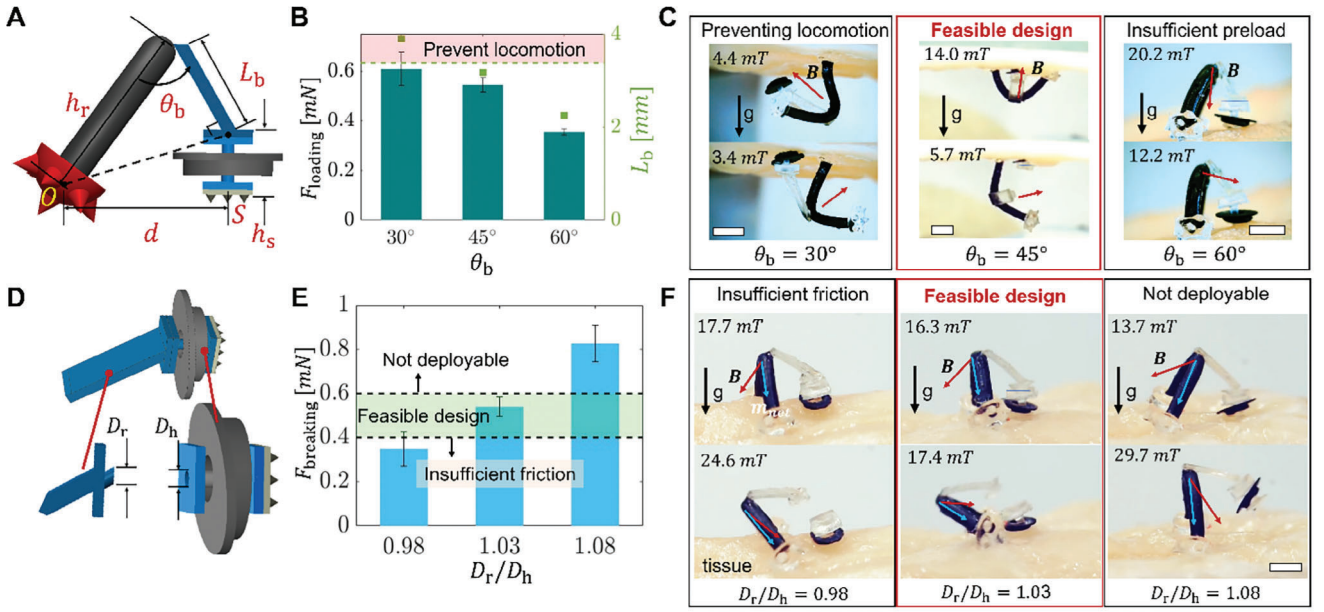


**Figure 3.** Design of the sensor delivery mechanism. A) Illustration of the dimensions of a soft robot for delivering a viscosity sensor. $\theta_b$: the angle between the robot body plane and the delivery beam. Point *O*: the midpoint between the two footpads. Point *S*: the loading point of the viscosity sensor. *d*: the distance between point *O* and *S*. $h_r$: the height of the robot body. $L_b$: the length of the delivery beam. $h_s$: the height of the viscosity sensor. B) The maximum loading force generated by robots with different $\theta_b$. The red shaded region indicates that the beam is too long and prevents robot locomotion. Error bars represent the standard deviation for $n = 3$ measurements. C) Images of the delivery process for robots with $\theta_b$ = 30°, 45° and 60°. The design marked by red box shows both sufficient loading force and robot climbing locomotion. Scale bars, 2 mm. D) Illustration of the delivery beam and the sensor with key design parameters. $D_r$: The diameter of the rod on the delivery beam. $D_h$: the diameter of the hole on the viscosity sensor. E) The required breaking force of the delivery beam and sensor with different $D_r/D_h$. The green area marks the desired breaking force for both reliable navigation and feasible release of the sensor based on a loading force of 0.6 mN. Error bars represent the standard deviation for $n = 3$ measurements. F) Video snapshots (Movie S2, Supporting Information) of the delivery process for robots with different $D_r/D_h$. Scale bars, 2 mm.

be 0.6 mN. Finally, when $D_r/D_h = 1.03$, the breaking force is sufficient to ensure controllable deployment as shown in Figure 3F.

### 2.3. Characterization of the Sensor Anchoring Force on Soft Biological Tissues

To further investigate the retention of the viscosity sensor on soft tissues, we quantify the anchoring force of the sensor on porcine colon tissues using a cantilever beam (Figure S4, Supporting Information) based on the Euler-Bernoulli beam theory in **Figure 4**. First, we quantify the normal anchoring force in Figure 4A–C. Figure 4A shows that a sensor probe attached to the tip of the cantilever beam is loaded on the porcine tissue. The displacement and the normal anchoring force calculated from the beam deflection $d_c$ in the detachment process are plotted in Figure 4B. We apply a preload of 0.39, 0.51, and 0.6 mN respectively to the sensor using the cantilever beam, which are the maximum loading forces for robots with different $\theta_b$ when having the same applied maximum magnetic torque. Figure 4C shows the maximum normal anchoring forces, where loading forces of 0.51 and 0.6 mN yield normal adhesion on the sensor patch that are larger than the breaking force thus allowing for sensor deployment. In contrast, a loading force of 0.39 mN cannot provide sufficient adhesion to the sensor patch that causes the sensor patch to detach from the tissue surface before the sensor is deployed. Furthermore, the anchoring performance is also tested when the viscosity sensor is exposed to mucus with phosphate buffered saline (PBS) and SGF for testing the effect of pH on sensor anchoring performance. As shown in Figure S5 (Supporting Information), the anchoring performance of the viscosity sensor is minimally affected because the adhesion between the sensor patch bioadhesive and mucus layer is not pH-responsive.

Moreover, in Figure 4D–F, we quantify the shear anchoring force when the cantilever beam exerts tangential forces to the sensor. Figure 4D shows that the sensor is first loaded onto the tissue surface by normal forces, and then a tangential force is applied on one side of the sensor patch by moving the cantilever beam. A force-displacement curve is plotted in Figure 4E, which shows that the sensor patch starts to slide on the tissue surface when the tangential force exceeds the maximum shear force. The maximum shear force for sensor patches with and without microspikes is compared in Figure 4F. The patch with microspikes has a shear retention force of 1.3 mN that is significantly larger than the 0.2 mN for the patch without spikes . The shear retention force is larger than the normal retention force because the spikes can penetrate the mucus layer and enable the chitosan to form stronger bonds with the mucus layer.

Lastly, we investigate the robustness of the sensor anchoring mechanism on soft tissues when subject to external disturbances. Figure 4G and Movie S3 (Supporting Information) demonstrate that the sensor can withstand a water flow up to 160 $mm^{-1}$ s before being flushed away which is larger than the maximum flow rate in the GI tract (76 $mm^{-1}$ s).[38] Meanwhile, Figure 4H and

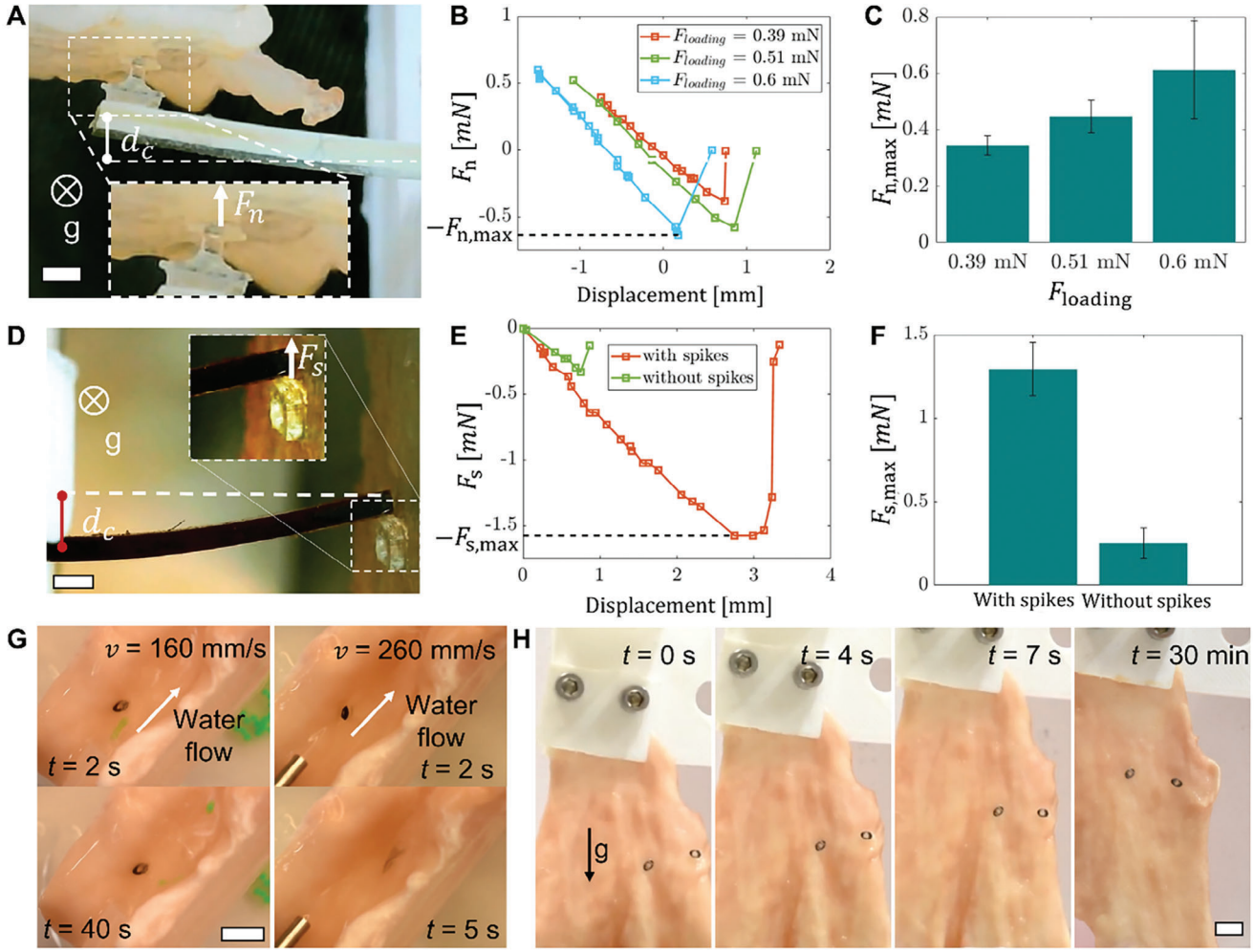


**Figure 4.** Characterization of the anchoring force on porcine colon tissues. A) Image of the experiment measuring the normal anchoring force of a viscosity sensor on porcine tissues. Scale bar, 1 mm. B) The normal anchoring forces for a sensor on porcine colon tissues under different preloads as a function of the cantilever beam displacement. C) The maximum normal anchoring force for a sensor on porcine colon tissues under different preloads. D) Image of the experiment measuring the shear anchoring force of a viscosity sensor on porcine tissues. Scale bar, 1 mm. E) The shear anchoring forces for sensors on porcine colon tissues with or without microspikes as a function of the cantilever beam displacement. F) The maximum normal anchoring force for sensors with spikes and without spikes on porcine colon tissues. G) Video snapshots (Movie S3, Supporting Information) of the sensor retention experiment on porcine tissues when flushed with water. Scale bar, 5 mm. H) Video snapshots (Movie S3, Supporting Information) of the anchored viscosity sensor when subject to a cyclic dynamic load on the tissue. Scale bar, 5 mm. In C and F, the error bars represent the standard deviation for $n = 3$ measurements.

Movie S3 (Supporting Information) show that the viscosity sensor remains on the porcine colon tissues when the colon tissue is exposed to cyclic loading at a frequency of 0.05 Hz, which is close to the peristaltic motion of the GI tract, through stretching and compressing the tissue by a mechanical tester.[39] These tests show the potential for the viscosity sensor to remain anchored on colon tissues for monitoring mucus properties despite unintentional and periodic disturbances.

### 2.4. Mechanism of Wirelessly Sensing Liquid Viscosity In Situ

In **Figure 5**, we present the mechanism of viscosity sensing by showing the theoretical derivation, calibration method, and sensing process of the viscosity sensor. After the sensor anchors on the mucus layer, the magnetic spinner will contact the mucus layer as shown in Figure 5A. The magnetic spinner, composed of a magnetic ring and a magnetic disk, is wetted by the mucus with the help of the capillary force. Figure 5B illustrates the viscosity sensing mechanism when a rotating external magnetic field is applied in the plane of the tissue surface. The moment balance equation of the magnetic spinner is given by,

$$\tau_m^s = \tau_d + \tau_f \tag{2}$$

where $\tau_m$, $\tau_d$, $\tau_f$ are the torques from magnetic fields, fluid drag, and other friction forces. The magnetic torque magnitude is given by $\tau_m^s = m_s\ Bsin(\theta_B - \theta_r)$, where $m_s$, $B$, $\Delta\theta = \theta_B - \theta_r$ are the magnetic moment of the spinner, the external magnetic field, and the angle difference between $\boldsymbol{B}$ and $\boldsymbol{m}_s$, respectively.

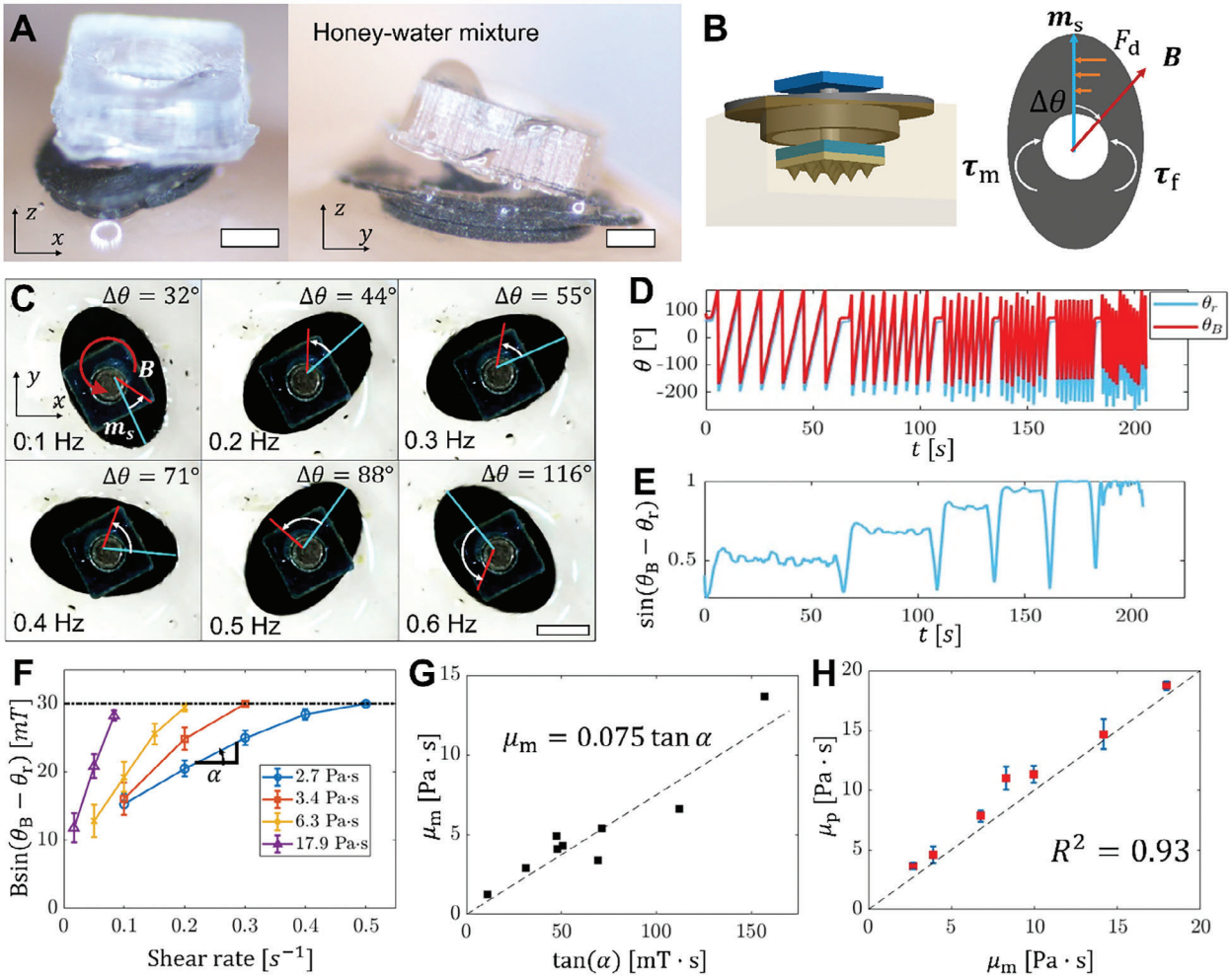


**Figure 5.** Characterization of viscosity sensing by the magnetically actuated viscosity sensor. A) Images of the experiment anchoring the viscosity sensor onto a mucus layer of porcine colon tissues. Scale bar, 500 μm. B) Illustration of the rigid-body torques, and forces applied on the magnetic spinner of the sensor. C) Images of the sensor spinning in a honey-water mixture actuated by a rotating external magnetic field of different frequencies. The measured viscosity of the honey-water mixture is $\mu_m = 2.7$ Pa s. Red line: magnetic field $B$. Blue line: magnetic moment of the magnetic spinner $m_s$. Scale bar, 1 mm. D) The orientation of the magnetic moment and external magnetic field for the viscosity sensing process. E) Sine of the angle difference between the magnetic field and magnetic moment for the viscosity sensing process. F) The calibration curve for the component of the external magnetic field normal to the magnetic moment of the sensor probe at different shear rate. The slope of the calibration curve is defined as $\tan(\alpha)$. Error bars represent standard deviation for $n = 5$ periods. G) The slope of the calibration curves for honey-water mixture with different viscosity. H) The predicted viscosity $\mu_p$ as a function of the measured viscosity $\mu_m$ for honey-water mixtures of different viscosities. The error bars represent the standard deviation for $n = 3$ measurements.

Meanwhile, assuming $\tau_d$ is proportional to the spinner rotating frequency with no step-out, we have $\tau_d = K_A \mu_f f_B$, where $K_A, \mu_f, f_B$ are the coefficient of the fluid drag, the dynamic viscosity of the liquid, and the magnetic field frequency, respectively. By substituting $\tau_d$ and $\tau_m^s$ in Equation 2, we have

$$B\sin\Delta\theta = \frac{K_A \mu_f}{m_s} f_B + \frac{\tau_f}{m_s} \tag{3}$$

In the sensing process, $\Delta\theta = \theta_B - \theta_r$ could be estimated via imaging. The coefficient of the fluid drag $K_A$ is assumed to be a constant dependent on the geometry of the magnetic spinner. The average friction-induced torque $\tau_f$ is assumed to be constant in each period. Therefore, the liquid dynamic viscosity at different shear rates can be determined by quantifying the curve slope angle when plotting $B\sin\Delta\theta$ as a function of the shear rate when $K_A/m_s$ and $\tau_f/m_s$ are known after calibration.

We further show the calibration and validation of the viscosity sensor in Figure 5C–H and Movie S4 (Supporting Information). We calibrate $K_A/m_s$ for every viscosity sensor with a magnetic spinner by placing the viscosity sensor in either glycerol or a honey-water mixture with known dynamic viscosities on a plastic substrate. The bottom surface of the magnetic spinner is fully wetted while the top surface remains above the liquid-air interface. A rotating magnetic field with a magnitude of 30 mT, generated by a permanent magnet, is applied to the spinner at different frequencies. $\Delta\theta$ is extracted from sequential optical images as shown in Figure 5C. As the frequency increases, $\Delta\theta$

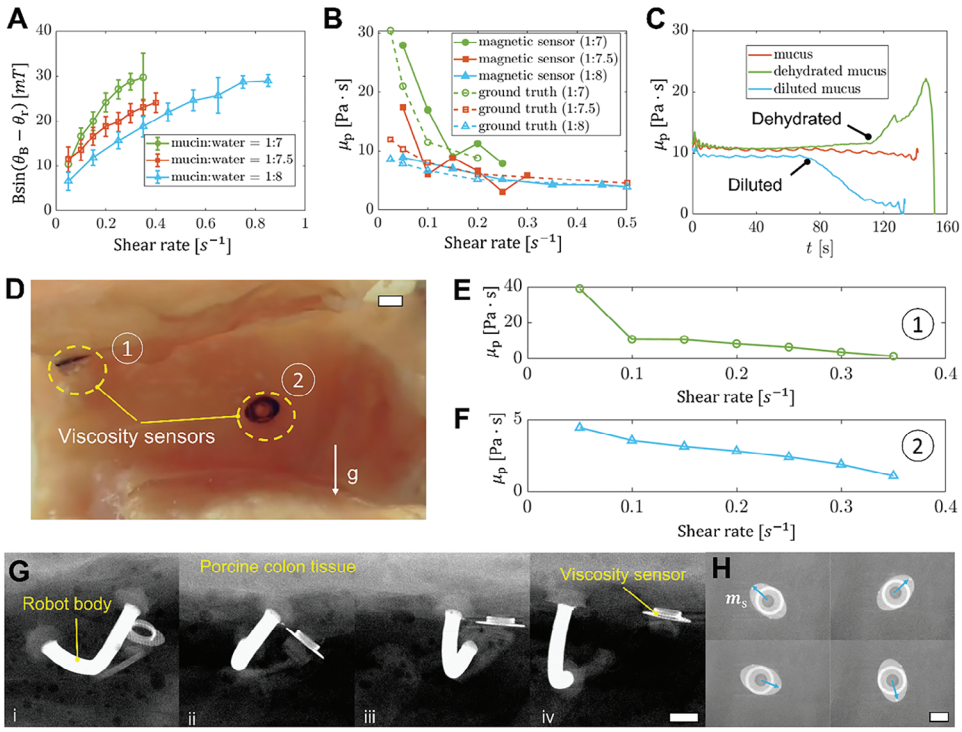


**Figure 6.** Sensing mucus viscosity on porcine tissues ex vivo and robot locomotion under X-ray imaging guidance. A) Sensor signal outputs as a function of the shear rate in mucus of varying water-mucin ratios. B) The predicted mucus viscosity using the magnetic viscosity sensor and the measured viscosity using a commercial viscometer as a function of the shear rate. Water-mucin mixtures used have different mixing ratios of 1:7, 1:7.5, and 1:8 (mucin and water by weight). C) The predicted time-varying mucus viscosity as a function of time with a shear rate of 0.15 $s^{-1}$. D) Video snapshot (Movie S4, Supporting Information) of the viscosity sensing process for two sensors deployed on the top and vertical surfaces of porcine colon tissues. Scale bar, 1 mm. E,F) The predicted mucus viscosity as a function of the shear rate for Sensor 1 (E) and Sensor 2 (F). G) Sequential X-ray medical images of the robot climbing porcine colon tissues and the sensor deployment process. i) climbing locomotion; ii) sensor loading; iii,iv) sensor detaching. H) Sequential X-ray medical images of the viscosity sensing process with the deployed viscosity sensor. In all figures, scale bars, 1 mm.

also increases when the required magnetic torque to overcome the fluid drag increases. After $\Delta\theta$ is larger than 90°, the spinner starts to step out meaning the magnetic torque cannot keep the magnetic spinner rotating at the same frequency as shown in Figure 5D,E. We further plot $B\sin\Delta\theta$ as a function of the shear rate when the shear rate increases until the magnetic spinner steps out as illustrated by the viscosity sensing curve in Figure 5F for the same sensor in liquids of various viscosities. To calibrate the sensor, Newtonian liquids with nine different viscosities are used. The viscosities varying from 1.3 to 13.7 Pa s are measured by a viscometer (Bonvoisin Digital Rotary Viscometer). To get $K_A/m_s$, the slopes of the viscosity sensing curves are extracted as shown in Figure 5G. To verify the calibration result, we compare the predicted and measured viscosities of another seven Newtonian liquids with viscosities from 2.7 to 17.9 Pa s. Figure 5H shows that the predicted viscosity agrees with the measured viscosity with a $R$ value of 0.93.

### 2.5. Medical Imaging-Guided Mucus Viscosity Sensing and Robot Locomotion

In **Figure 6**, we demonstrate the potential of using the viscosity sensor to sense mucus viscosity in situ. First, we prepare porcine mucus by mixing porcine mucin and water when three different mucin-water ratios with different shear-rate dependent viscosities are prepared. The slopes of the viscosity sensing curves decrease as the shear rate increases in Figure 6A. When using a shear rate from 0.05 to 0.5 $s^{-1}$, the mucus displays shear-thinning behavior. Then, the calibration data is used to predict the mucus viscosity of different mucin-water ratios at different shear rates as shown in Figure 6B. Additionally, the viscosity sensor is tested with mucus (1:8 mucin-water ratio in weight) mixed with PBS and SGF. As shown in Figure S6 (Supporting Information), the SGF has a negligible effect on the viscosity sensing curve of the sensor as the sensing mechanism relies on fluid-structure interaction rather than pH.

The temporal sensing capabilities of the viscosity sensor are shown in Figure 6C where the mucus viscosity is varied and monitored. The first experiment is conducted with mucus at a 1:7 mucin-water ratio in weight and constant shear rate of 0.15 $s^{-1}$, when the predicted viscosity stays constant. Further experiments are modified to increase or decrease the mucus viscosity. To decrease the viscosity, the mucus is diluted, and the predicted viscosity shows a corresponding decrease. On the other hand, the mucus viscosity is increased by dehydrating the mucus through heating at 90 °C, and the predicted viscosity shows a corresponding increase. Equation 3 is used to calculate the viscosity, where $\tau_f$ is acquired from previous mucus viscosity sensing experiment and assumed to be constant in each period. The ability to

temporally sense viscosity allows monitoring physiological and pathophysiological conditions for disease diagnosis.

Moreover, to spatially sense viscosity, we demonstrate the potential in building a sensor network where multiple sensors are deployed at different locations as shown in Figure 6D–F and Movie S4 (Supporting Information). As a proof-of-concept, two sensors are loaded on the top and vertical surfaces of a porcine colon tissue ex vivo. Mucus with different viscosities are applied locally to where the viscosity sensors are loaded. By applying a rotating magnetic field sequentially in the sensor spinner plane, the local liquid viscosity could be sensed at specific locations as shown in Figure 6E,F.

Finally, we demonstrate that the soft climbing robot and the viscosity sensor can be tracked and guided with medical imaging guidance in the GI tract as displayed in Figure 6G,H. We prepare a tubular phantom with porcine colon tissue attached to the inner surface of the tube (see Figure S7, Supporting Information). The soft climbing robot with a magnetic viscosity sensor is deployed on the tissue surface before the X-ray imaging. The robot locomotion and sensor deployment are demonstrated with the X-ray imaging as shown in Figure 6G. The external magnetic field can be controlled to navigate the robot based on the feedback of the robot position and shape. Once the viscosity sensor is loaded on the mucus layer, we can provide a rotating magnetic field using a permanent magnet mounted on a rotational and translational motion stage and track the sensor with X-ray imaging. The magnetic moment for the elliptical spinner on the sensor is along its major axis and can be tracked clearly using the X-ray imaging as shown in Figure 6H.

## 3. Discussion

In summary, we have proposed a delivery mechanism for wireless miniature sensors on mucus-covered tissue surfaces by designing, fabricating, and controlling millimeter-scale soft climbing robots and magnetically actuated viscosity sensors based on fluid-structure interaction. We have shown that a millimeter-scale soft climbing robot can be actuated by magnetic fields to have omni-directional steering ability for climbing mucus-covered tissues and loading viscosity sensors on the soft tissues. The adhesive patch on the viscosity sensor allows for prolonged retention of the sensor on soft tissues for hours. The magnetic viscosity sensor, actuated by magnetic fields and tracked by medical imaging, has been shown to sense the viscosity of both synthetic and biological Newtonian and non-Newtonian fluids. Finally, we have demonstrated controlling the soft robot to deliver multiple viscosity sensors on the porcine colon tissues ex vivo to sense mucus viscosities spatiotemporally.

Compared with other viscosity sensing devices (see Table S2, Supporting Information), our wireless miniature viscosity sensor could be deployed at target locations on biological tissues with a relatively long retention, which could be potentially used for in vivo applications. In contrast, most viscosity sensors based on piezoelectric vibrators[40–43] are tethered which cannot be used for long-term monitoring inside the body. Other viscosity sensors based on optical[44] or capillary[45–47] effect rely on bulky light control units and microfluidic channels, respectively, which have only been shown for in vitro applications, limiting their application for in vivo environments. Lastly, magnetic nanowire[33] has been shown to sense mucus viscosity by combining optical imaging in vitro but it lacks the ability of long-term retention on biological tissues for in vivo applications.

Toward long-term viscosity sensing, the retention time of the viscosity sensor on soft tissues could be increased, which is currently limited by the turn-over time of the mucus which is typically several hours. The retention time could be increased if integrated with mechanical anchoring mechanism such as a swelling hydrogel[48] or heat-triggered gripper.[49] To allow biocompatibility of the robot and sensor, the following possible methods could be used. First, the biocompatibility of the robot and sensors could be realized by coating a thin layer of PDMS[50] or parylene C.[51] Parylene C has been shown to allow a biocompatible coating when there are no cracks. The bending motion of our robot induce a strain up to 10% which is less likely to cause the crack. In addition, as the only non-biocompatible material is the NdFeB particles, we could further coat the NdFeB particles with silicon dioxide (silica) to allow biocompatibility.[52,53] Preliminary leaching test suggested that the silica coating could prevent the NdFeB particles from leaching (see Figure S8, Supporting Information) and could potentially allow enhanced biocompatibility though further cell toxicity test needs to be completed to validate the biocompatibility. As a future work, we will perform long-term biocompatibility test for the robot and viscosity sensor after coating them with PDMS and parylene C and performing silica-coating for the NdFeB particles.

We will also perform in vivo test of the robot and viscosity sensor in porcine organs to further validate the effectiveness of the delivery and sensing mechanism. Nonetheless, the omnidirectional climbing ability of our soft climbing robot allows delivery of the viscosity sensors on locations that are challenging to reach in the GI tract, enabling targeted delivery of sensors precisely at different GI tract locations for building a sensor network by sequentially sending multiple soft climbing robots. Moreover, the magnetic actuation of the sensor and medical imaging-based motion tracking allow sensing at locations deep inside the body.[54] In addition, although we demonstrate the delivery of viscosity sensors in this work, the proposed sensor delivery mechanism could also be used for delivering other wireless sensors for sensing temperature,[34] pH,[35] and other physiological properties. Our work could inspire other soft miniature robots driven by magnetic fields[55] and other untethered soft robots[56] for targeted delivery of versatile sensors in confined environments for building a sensor network. The proposed method thus paves the way toward long-term, continuous monitoring and minimally invasive tracking physiological properties to help understand disease development and provide early diagnosis.

## 4. Experimental Section

*Fabrication of the Robot Body*: The 3D soft climbing robot capable of delivering viscosity sensors on soft biological tissues consists of a magnetic robot body, two half-spherical footpads, and a delivery beam. The robot body was made by injection molding. Ecoflex 00–30 silicone rubber (Smooth-On Inc.), Ecoflex silicone gel (Smooth-On Inc.), and NdFeB microparticles (average diameter, 5 μm; MQFP-15-7, Neo Magnequench) were mixed at a 3:1:8 ratio by weight and then poured into a syringe. The mixture was injected into a polyimide tube with an inner diameter of 740 μm and cured at room temperature. The cured mixture was cut into

8-mm long segments and extracted from the polyimide tube. The robot body was then attached to a piece of Scotch tape, folded into a "U"-shape, and magnetized in an impulse magnetizer (IM-10-30, ASC Scientific) with a 1.8 T magnetic field impulse.

*Fabrication of the Robot Footpads*: The robot footpads were made by transfer molding. First, positive molds for the half-spherical footpads were printed using clear resin (Formlabs, Inc) in a 3D resin printer (Form 3+, Formlabs, Inc.). After printing, the molds were cleaned in isopropyl alcohol in an ultrasonic cleaner for 20 mins. Subsequently, the molds were exposed to UV light (wavelength: 365 nm) to cure for 15 min. The positive molds were then coated with Trichloro(1H,1H,2H,2H-perfluorooctyl)silane (97%, Sigma–Aldrich, Inc.) by vacuum deposition. Then, negative molds were made with polydimethylsiloxane (PDMS, Dow Silicones Corporation) with a weight ratio of 10:1 between the monomer to the cross-linker (denoted as 10:1 PDMS in the following text) through casting the positive mold. The 10:1 PDMS was vacuumed and then cured on the hotplate at 90 °C for 1 h. The negative molds were further coated with Trichloro(1H,1H,2H,2H-perfluorooctyl)silane. The 10:1 PDMS was cast into the negative mold and cured on a hotplate at 90 °C for 30 mins to obtain the half-spherical footpads. Two footpads were then glued on the robot body using uncured 10:1 PDMS with the assistance of a 3D-printed jig. Finally, the footpads were coated with Poly(ethylene glycol) Diacrylate (PEGDA) to enable the chitosan-based bio-adhesive to adhere to its surface. Benzophenone solution (20 wt.% in ethyl alcohol, Sigma–Aldrich Inc.) was pipetted over the footpads as the hydrophobic photo-initiator. The mixture of PEGDA and deionized water at a 20% weight ratio combined with $\alpha$-ketoglutaric acid (Chem-Impex Int'l. Inc.) at a 1% weight ratio was then added on the footpads and cured using a UV lamp (365 nm) for 15 mins.

*Fabrication of the Sensor Delivery Structure*: The delivery beam is composed of a long beam, a square sheet, and a tilted rod for connecting to the sensor, all made of 10:1 PDMS. To make the beam, a glass substrate was prepared with a 150-µm-thick spacer. 10:1 PDMS was poured onto the substrate and scraped with a razor blade. The scraped PDMS was then cured in an oven at 90 °C for 20 mins. The cured PDMS sheet was cut into rectangular beams of 1.2 mm in width and different lengths, as well as 1.2 mm by 1.2 mm by 120 µm square sheets using a laser machine (LPKF ProtoLaser U4, LPKF Laser & Electronics North America). To make the delivery beam stiff for ease of sensor deployment, uncured 10:1 PDMS was used to glue three thin PDMS beams together and cured at 90 °C. The square-shaped PDMS sheet was attached to the stacked PDMS beam at an angle of 60°. The tilted shaft was fabricated with the same transfer molding method used for fabricating the robot footpads. The tilting angle of 60° is designed to allow easy detachment of the sensor. The connecting rod has a length of 0.3 mm and a diameter varying from 0.56 to 0.66 mm. The cured tilting rod was further glued onto the square PDMS sheet. The delivery beam was then adhered to the robot body with a specific angle assisted by a 3D-printed jig.

*Fabrication of the Viscosity Sensor*: The viscosity sensor consists of a top stopper with a tilted hole, a PDMS shaft, a magnetic spinner, and a bottom adhesive patch with microspikes. As shown in Figure S2 (Supporting Information), a negative mold for the square-shaped top stopper was printed using a 3D resin printer (Form 3+, Formlabs Inc.) and coated with Trichloro(1H,1H,2H,2H-perfluorooctyl)silane. The length and thickness of the stopper and the depth of the hole were 1.5, 0.5, and 0.3 mm respectively. The 10:1 PDMS was cast on the negative mold and cured on the hotplate at 80 °C for 60 mins. The PDMS shaft was made by injection molding. The uncured 10:1 PDMS was poured into a syringe with 22 gauge needle whose inner diameter was 0.413 mm. Heat gun was used to cure the PDMS in the needle at 90 °C for 1 min. The cured shaft was then cut into segments with 0.5 mm in length using a razor blade. The bottom adhesive patch with microspikes was fabricated through the same transfer molding method used for making robot footpads. The positive mold with a 7-by-7 microspike matrix was printed by a 3D printer based on two-photon photolithography (Photonic Professional GT, NanoScribe). After casting and curing the 10:1 PDMS on the negative mold, the PDMS sheet with microspikes was cut into a disk of 1.1 mm in diameter with the LPKF U4 laser machine for integrating on the bottom adhesive patch. To make the magnetic spinner, 10:1 PDMS and NdFeB particles were mixed at a 1:2 ratio by weight and poured onto a glass substrate with a 150-µm-thick spacer. After being scraped and cured in an oven at 90 °C for 20 mins, the magnetic PDMS sheet was cut into ellipse-shaped disks with the long diameter of 2.4 mm and the short diameter of 1.6 mm. Two laser-cut magnetic rings with an outer diameter of 1.6 mm and an inner diameter of 1.2 mm were glued to the elliptical magnetic disk using uncured 10:1 PDMS. The assembled magnetic spinner was then magnetized along the long-diameter axis in a 0.74 T magnetic field impulse using an impulse magnetizer (IM-10-30, ASC Scientific). The top stopper, the PDMS shaft, the magnetic spinner, and the bottom adhesive patch were glued together to make the viscosity sensor. The bottom adhesive patch with microspikes was then coated with hydrogel and applied bioadhesive.

*Magnetic Actuation*: The two magnetic actuation systems in the experiments include an electromagnetic actuation system and a mobile permanent magnet system as shown in Figure S9 (Supporting Information). The electromagnet system had six solenoids in a half-spherical configuration to allow a large workspace of 7 cm by 7 cm by 1.5 cm with a 95% uniformity and a magnetic field strength up to 20 mT. The solenoids were driven by six DC motor drivers (Syren 50, Dimension Engineering). The motor drivers were powered by six DC power supplies (24 V, 20 A). A PCI board (PCIe-6738, National Instrument) was integrated in a PC and controlled by LabVIEW 2020 via a joystick or by a preprogrammed signal generator. The magnetic field in the workspace was measured using a 3-axis magnetic field sensor (TLE493D, Infineon, AG). Two cameras (ELP 5–50 mm Varifocal Lens 1080P USB Camera) were connected to the same PC for visualizing and recording the experimental videos simultaneously. In addition, a separate customized setup with permanent magnets mounted on a set of step motors was also used to test the robot when a stronger magnetic field up to 30 mT is needed or in experiments inside the X-ray medical imaging cabinet (Faxitron – MX-20). A permanent magnet was mounted on two stepper motors whose axes were perpendicular to each other. The magnet and step motors were further mounted on a linear motion stage controlled by another stepper motor. Two rotational step motors mounted on a linear motion stage were able to generate the desired 3D magnetic field. The magnet mounted on the two step motors were controlled for a desired magnetic field angle. The linear actuator allows moving the magnet to control the magnetic field magnitude.

*Preparing Bioadhesive*: To integrate the bio-adhesive onto the footpads, a bridging polymer chitosan (high molecular weight, Sigma–Aldrich Inc.) was dissolved into the compound 2-(N-morpholino)ethanesulfonic acid (MES) buffer (Sigma–Aldrich Inc.) at a weight ratio of 2.0%. 1 M NaOH was used to adjust the pH to ≈6 at a volume ratio of 0.13%. Unsulfated N-hydroxysuccinimide (NHS 98%, Sigma–Aldrich Inc.) was used as a coupling reagent with a concentration of 12 mg $mL^{-1}$ in the final solution.

*Preparing Porcine Tissues, Synthetic Liquids, and Mucus*: The fresh porcine colon tissues were purchased from a local slaughterhouse . The tissue was kept frozen in the freezer and defrosted before experiments. The porcine tissue was cut and attached to glass slides for testing. Pure glycerol, honey-water mixture, and synthetic mucus were used for experiments. Honey-water mixture was made by mixing honey and water at 100:1, 75:1, 50:1, and 25:1 ratios by volume, respectively. For the synthetic mucus, mucin from porcine stomach (Type II, 88%, Chem-impex International Inc.) was added into deionized water at 1:6, 1:7.5, 1:8 ratios by weight, respectively. The mixture was then stirred for 1 h at room temperature.

*Preparing Cantilever Beam for Characterizing the Sensor Anchoring Forces*: To prepare the cantilever beam for quantifying the robot-tissue adhesion, Mold Max-40 (Smooth-On Inc.) and MoldMax-60 (Smooth-On Inc.) were poured onto an acrylic glass substrate with a 700-µm-thick spacer. The uncured material was scraped with a razor blade and cured on the hotplate at 80 °C for 2 h. Subsequently, the Mold Max-40 and Mold Max-60 were cut into beams of 12.5 mm by 5 mm by 700 µm (length by width by thickness) using the LPKF U4 laser machine. For the normal anchoring force test, a viscosity sensor without the magnetic spinner was glued on the tip of the cantilever beam made of Mold Max-40. The beam was clamped with a 3D printed clamper and connected to a linear motion stage

controlled by a step motor as shown in Figure S4 (Supporting Information). The sensor was first pushed against the porcine colon tissue with a controlled displacement of the clamper and thus a controlled loading force for about1.5 mins. The beam was then slowly pulled away from the tissue until the sensor was fully detached from the tissue surface. For the shear anchoring force, a viscosity sensor without the magnetic spinner or the PDMS shaft was first loaded on porcine colon tissues using the Mold Max-60 beam controlled by a linear motion stage. The sensor was pushed against the porcine colon tissue similar to the normal anchoring force test, with a controlled displacement of the clamper to apply the desired loading force for 1.5 mins. After loading, the cantilever beam rotated 90 degrees so that it could apply a shear force on the sensor for quantifying the shear anchoring force.

## Supporting Information

Supporting Information is available from the Wiley Online Library or from the author.

## Acknowledgements

The authors would like to thank the funding support from the Vanderbilt University School of Engineering and Vanderbilt Institute for Surgery and Engineering. The authors also would like to thank Oak Ridge National Laboratory for the facility support on material characterization. The co-authors name (L.B.) was corrected after initial online publication.

## Conflict of Interest

The authors declare no conflict of interest.

## Data Availability Statement

The data that support the findings of this study are available in the supplementary material of this article.

## Keywords

gastrointestinal tract mucus, magnetic actuation, miniature soft robot, minimally invasive, sensing

Received: July 6, 2023
Revised: October 23, 2023
Published online:

[1] K. Nan, V. R. Feig, B. Ying, J. G. Howarth, Z. Kang, Y. Yang, G. Traverso, *Nat. Rev. Mater.* **2022**, *7*, 908.
[2] L. A. Beardslee, G. E. Banis, S. Chu, S. Liu, A. A. Chapin, J. M. Stine, P. J. Pasricha, R. Ghodssi, *ACS Sens.* **2020**, *5*, 891.
[3] S. K. Lai, Y.-Y. Wang, D. Wirtz, J. Hanes, *Adv. Drug Deliv. Rev.* **2009**, *61*, 86.
[4] M. Herath, S. Hosie, J. C. Bornstein, A. E. Franks, E. L. Hill-Yardin, *Front Cell Infect. Microbiol.* **2020**, *10*, 248.
[5] C. E. Wagner, K. M. Wheeler, K. Ribbeck, *Annu. Rev. Cell Dev. Biol.* **2018**, *34*, 189.
[6] F. Taherali, F. Varum, A. W. Basit, *Adv Drug Deliv Rev* **2018**, *124*, 16.
[7] F. Younan, J. Pearson, A. Allen, C. Venables, *Gastroenterology* **1982**, *82*, 827.
[8] J. R. N. Curt, R. Pringle, *Gut* **1969**, *10*, 931.
[9] M. E. V. Johansson, *Inflamm Bowel Dis* **2014**, *20*, 2124.
[10] E. S. Corazziari, *J. Pediatr. Gastroenterol. Nutr.* **2009**, *48*, S54.
[11] P. Paone, P. D. Cani, *Gut* **2020**, *69*, 2232.
[12] R. C. De Lisle, D. Borowitz, *Cold Spring Harb. Perspect. Med.* **2013**, *3*, a009753.
[13] J. H. Hageman, M. C. Heinz, K. Kretzschmar, J. Van Der Vaart, H. Clevers, H. J. G. Snippert, *Dev. Cell* **2020**, *54*, 435.
[14] T. Kelly, J. Buxbaum, *Dig. Dis. Sci.* **2015**, *60*, 1903.
[15] J. Dorsey, T. Gonska, *J. Cystic Fibrosis* **2017**, *16*, S14.
[16] P. Korc, S. Sherman, *Gastrointest. Endosc.* **2016**, *84*, 557.
[17] I. Boskoski, G. Costamagna, *Digestive Endoscopy* **2019**, *31*, 119.
[18] R. Rudiman, *Annals of Med. Surg.* **2021**, *71*, 102922.
[19] K. J. Wernli, A. T. Brenner, C. M. Rutter, J. M. Inadomi, *Gastroenterology* **2016**, *150*, 888.
[20] K. Kalantar-Zadeh, K. J. Berean, N. Ha, A. F. Chrimes, K. Xu, D. Grando, J. Z. Ou, N. Pillai, J. L. Campbell, R. Brkljaca, K. M. Taylor, R. E. Burgell, C. K. Yao, S. A. Ward, C. S. Mcsweeney, J. G. Muir, P. R. Gibson, *Nat. Electron.* **2018**, *1*, 79.
[21] J. Z. Ou, C. K. Yao, A. Rotbart, J. G. Muir, P. R. Gibson, K. Kalantar-Zadeh, *Trends Biotechnol.* **2015**, *33*, 208.
[22] H. Rezaei Nejad, B. C. M. Oliveira, A. Sadeqi, A. Dehkharghani, I. Kondova, J. A. M. Langermans, J. S. Guasto, S. Tzipori, G. Widmer, S. R. Sonkusale, *Adv. Intelli. Sys.* **2019**, *1*, 1900053.
[23] J. F. Waimin, S. Nejati, H. Jiang, J. Qiu, J. Wang, M. S. Verma, R. Rahimi, *RSC Adv.* **2020**, *10*, 16313.
[24] F. Soto, E. Purcell, M. O. Ozen, P. D. Sinawang, J. Wang, D. Akin, U. Demirci, *Adv. Intelli. Sys.* **2022**, *4*, 2200030.
[25] N. Shamsudhin, V. I. Zverev, H. Keller, S. Pane, P. W. Egolf, B. J. Nelson, A. M. Tishin, *Med. Phys.* **2017**, *44*, e91.
[26] M. Mimee, P. Nadeau, A. Hayward, S. Carim, S. Flanagan, L. Jerger, J. Collins, S. Mcdonnell, R. Swartwout, R. J. Citorik, V. Bulovic, R. Langer, G. Traverso, A. P. Chandrakasan, T. K. Lu, *Science* **2018**, *360*, 915.
[27] A. F. Hagel, E. Gäbele, M. Raithel, W. H. Hagel, H. Albrecht, T. M. De Rossi, C. Singer, T. Schneider, M. F. Neurath, M. J. Farnbacher, *Can J. Gastroenterol. Hepatol.* **2014**, *28*, 77.
[28] H. M. Kim, S. Yang, J. Kim, S. Park, J. H. Cho, J. Y. Park, T. S. Kim, E.-S. Yoon, S.i Y. Song, S. Bang, *Gastrointest. Endosc.* **2010**, *72*, 381.
[29] M. Quirini, S. Scapellato, P. Valdastri, A. Menciassi, P. Dario, In **2007**, *2007 29th Annual International Conference of the IEEE Engineering in Medicine and Biology Society*, IEEE, pp. 2827–2830.
[30] X. Du, K. F. Chan, X. Xia, P. W. Y. Chiu, L. Zhang, In **2018**, *2018 IEEE International Conference on Cyborg and Bionic Systems (CBS)*, IEEE, pp. 250.
[31] M. Mimee, P. Nadeau, A. Hayward, S. Carim, S. Flanagan, L. Jerger, J. Collins, S. Mcdonnell, R. Swartwout, R. J. Citorik, V. Bulovic, R. Langer, G. Traverso, A. P. Chandrakasan, T. K. Lu, *Science* **2018**, *360*, 915.
[32] A. Moglia, A. Menciassi, P. Dario, A. Cuschieri, *Nat. Rev. Gastroenterol. Hepatol.* **2009**, *6*, 353.
[33] M. Radiom, R. Hénault, S. Mani, A. G. Iankovski, X. Norel, J.-F. Berret, *Soft Matter* **2021**, *17*, 7585.
[34] C. Shi, V. Andino-Pavlovsky, S. A. Lee, T. Costa, J. Elloian, E. E. Konofagou, K. L. Shepard, *Sci. Adv.* **2021**, *7*.
[35] J. E. Pandolfino, P. J. Kahrilas, *Gastrointest. Endosc. Clin. N Am.* **2005**, *15*, 307.
[36] Y. Wu, X. Dong, J. Kim, C. Wang, M. Sitti, *Sci. Adv.* **2022**, *8*, eabn3431.
[37] J. Li, A. D. Celiz, J. Yang, Q. Yang, I. Wamala, W. Whyte, B. R. Seo, N. V. Vasilyev, J. J. Vlassak, Z. Suo, D. J. Mooney, *Science* **2017**, *357*, 378.
[38] M. J. Ferrua, R. P. Singh, *J. Food Sci.* **2010**, *75*, R151.
[39] J. D. Huizinga, J.i-H. Chen, Y. Fang Zhu, A. Pawelka, R. J. Mcginn, B. L. Bardakjian, S. P. Parsons, W. A. Kunze, R. Y. Wu, P. Bercik, A.

Khoshdel, S. Chen, S. Yin, Q. Zhang, Y. Yu, Q. Gao, K. Li, X. Hu, N. Zarate, P. Collins, M. Pistilli, J. Ma, R. Zhang, D. Chen, *Nat. Commun.* **2014**, *5*, 3326.
[40] T. Manzaneque, V. Ruiz-Díez, J. Hernando-García, E. Wistrela, M. Kucera, U. Schmid, J. L. Sánchez-Rojas, *Sens. Actuators A Phys.* **2014**, *220*, 305.
[41] B. Jakoby, R. Beigelbeck, F. Keplinger, F. Lucklum, A. Niedermayer, E. K. Reichel, C. Riesch, T. Voglhuber-Brunnmaier, B. Weiss, *IEEE Trans. Ultrason. Ferroelectr. Freq. Control* **2010**, *57*, 111.
[42] T.-V. Nguyen, M.-D. Nguyen, H. Takahashi, K. Matsumoto, I. Shimoyama, *Lab Chip* **2015**, *15*, 3670.
[43] P. Soltani Zarrin, F. Jamal, S. Guha, J. Wessel, D. Kissinger, C. Wenger, *Biosensors* **2018**, *8*, 78.
[44] S. Yuan, Q. Zheng, B. Yao, M. Wen, W. Zhang, J. Yuan, H. Lei, *Biomed. Opt. Express* **2022**, *13*, 1152.
[45] P. S. Venkateswaran, A. Sharma, S. Dubey, A. Agarwal, S. Goel, *IEEE Sens. J.* **2016**, *16*, 3000.
[46] B. J. Kim, S. Y. Lee, S. Jee, A. Atajanov, S. Yang, *Sensors* **2017**, *17*, 1442.
[47] I. Jang, K. E. Berg, C. S. Henry, *Sens Actuators B Chem* **2020**, *319*, 128240.
[48] S. Y. Yang, E. D. O'cearbhaill, G. C. Sisk, K. M. Park, W. K. Cho, M. Villiger, B. E. Bouma, B. Pomahac, J. M. Karp, *Nat. Commun.* **2013**, *4*, 1702.
[49] A. Ghosh, L. Li, L. Xu, R. P. Dash, N. Gupta, J. Lam, Q. Jin, V. Akshintala, G. Pahapale, W. Liu, A. Sarkar, R. Rais, D. H. Gracias, F. M. Selaru, *Sci. Adv.* **2020**, *6*.
[50] S. L. Peterson, A. Mcdonald, P. L. Gourley, D. Y. Sasaki, *J. Biomed. Mater. Res.* **2005**, *72A*, 10.
[51] M. Golda-Cepa, K. Engvall, M. Hakkarainen, A. Kotarba, *Prog. Org. Coat.* **2020**, *140*, 105493.
[52] Y. Kim, G. A. Parada, S. Liu, X. Zhao, *Ferromag. Soft Continuum Robots* **2019**, *4*.
[53] Y. Kim, X. Zhao, *Am. Chem. Soc.* **2022**, *122*, 5317.
[54] M. Lin, H. Hu, S. Zhou, S. Xu, *Nat. Rev. Mater.* **2022**, *7*, 850.
[55] Y. Kim, X. Zhao, *Chem. Rev.* **2022**, *122*, 5317.
[56] S. I. Rich, R. J. Wood, C. Majidi, *Nat. Electron.* **2018**, *1*, 102.